Nature Chemistry, 2014,6,468-476 2014 DOI: 10.1038/NCHEM.1939

Functional carbon nanosheets prepared from hexayne amphiphile monolayers at room temperature

Stephen Schrettl[1], Cristina Stefaniu[2], Christian Schwieger[3], Guillaume Pasche[4], Emad Oveisi[4,5], Yannik Fontana[6], Anna Fontcuberta i Morral[6], Javier Reguera[7], Riccardo Petraglia[8], Clémence Corminboeuf[8], Gerald Brezesinski[2] and Holger Frauenrath[1]*

Carbon nanostructures that feature two-dimensional extended nanosheets are important components for technological applications such as high-performance composites, lithium-ion storage, photovoltaics and nanoelectronics. Chemical functionalization would render such structures better processable and more suited for tailored applications, but typically this is precluded by the high temperatures needed to prepare the nanosheets. Here, we report direct access to functional carbon nanosheets of uniform thickness at room temperature. We used amphiphiles that contain hexayne segments as metastable carbon precursors and self-assembled these into ordered monolayers at the air/water interface. Subsequent carbonization by ultraviolet irradiation in ambient conditions resulted in the quantitative carbonization of the hexayne sublayer. Carbon nanosheets prepared in this way retained their surface functionalization and featured an sp^2-rich amorphous carbon structure comparable to that usually obtained on annealing above 800 °C. Moreover, they exhibited a molecularly defined thickness of 1.9 nm, were mechanically self-supporting over several micrometres and had macroscopic lateral dimensions on the order of centimetres.

Two-dimensional (2D) carbon nanostructures, including graphene[1,2] and carbon nanosheets[3,4], are of high interest for fundamental studies of the physics of organic electronic materials[5,6], for novel types of nanocomposites or nanomembranes[7], as well as for use in capacitors[8,9], actuators[10] and sensors[11]. The processing of materials and possible applications, such as stimuli-responsive actuation or selective sensing, would benefit from chemical functionalization[12–15]. The direct access to tailored, dispersible materials with controlled surface chemistry, however, is impeded by the typical methods of preparation that use either exfoliation techniques[1] or high-energy processes[16,17]. Beyond the partial functionalization by postsynthetic chemical modification[12,18–20] or supramolecular approaches[12,21,22], recently Gölzhäuser, Turchanin and co-workers reported an elegant approach in which crosslinking of self-assembled monolayers by electron irradiation furnished carbon nanosheets that were pyrolysed further at elevated temperatures to yield partially functionalized graphene[3,4]. An improved strategy towards functional carbon nanosheets ought to start from similarly simple methods to prepare defined thin films using metastable molecular carbon precursors that can be carbonized under more benign conditions. In this regard, the air/water interface[23,24] provides a perfectly flat substrate that has been used in the straightforward preparation of self-assembled monolayers from reactive amphiphiles[25–28]. Oligoynes have already been used as molecular precursors in the low-temperature preparation of carbon nanostructures in bulk and in solution[29–31]. Reactive polydiacetylene nanofibres have been carbonized at room temperature[32], and recently carbon-rich monomers with multiple diacetylene functions were polymerized and graphitized at low temperature without control over the nanoscopic morphology to obtain micrometre-sized flakes of a multilayered graphitic material[33].

Here we combined different aspects of these previous research efforts into a novel approach for the 'bottom-up' preparation of functional carbon nanosheets at room temperature. To this end, we prepared the novel hexayne amphiphile **1** (Fig. 1a) as a reactive, carbon-rich sibling of typical fatty acid ester amphiphiles that formed well-ordered self-assembled monolayers at the air/water interface. Extensive structural investigations in combination with density functional theory (DFT) computations allowed us to obtain a detailed molecular model of the hexayne packing (Fig. 1b), which indicated that the oligoynes were densely packed into a <7 Å thick carbon-rich sublayer suitable for carbonization (Fig. 1c). Quantitative carbonization was then achieved by ultraviolet irradiation, which furnished self-supporting carbon nanosheets that comprised more than 80% graphitic carbon centres and a hydrophilic surface decoration.

Results and discussion

The hexayne amphiphile **1** was synthesized straightforwardly in five steps starting from hexynoic acid and using a recently developed

[1]Ecole Polytechnique Fédérale de Lausanne (EPFL), Institute of Materials, Laboratory of Macromolecular and Organic Materials, EPFL STI IMX LMOM, MXG 037, Station 12, 1015 Lausanne, Switzerland, [2]Max Planck Institute of Colloids and Interfaces, Department of Interfaces, 14476 Potsdam, Germany, [3]Martin Luther Universität Halle-Wittenberg, Institute of Chemistry, 06120 Halle (Saale), Germany, [4]Ecole Polytechnique Fédérale de Lausanne (EPFL), Interdisciplinary Centre for Electron Microscopy, 1015 Lausanne, Switzerland, [5]Ecole Polytechnique Fédérale de Lausanne (EPFL), Institute of Condensed Matter Physics, Electron Spectrometry and Microscopy Laboratory, 1015 Lausanne, Switzerland, [6]Ecole Polytechnique Fédérale de Lausanne (EPFL), Institute of Materials, Laboratory of Semiconductor Materials, 1015 Lausanne, Switzerland, [7]Ecole Polytechnique Fédérale de Lausanne (EPFL), Institute of Materials, Supramolecular Nanomaterials and Interfaces Laboratory, 1015 Lausanne, Switzerland, [8]Ecole Polytechnique Fédérale de Lausanne (EPFL), Institute of Chemical Sciences and Engineering, Laboratory for Computational Molecular Design, 1015 Lausanne, Switzerland. *e-mail: holger.frauenrath@epfl.ch

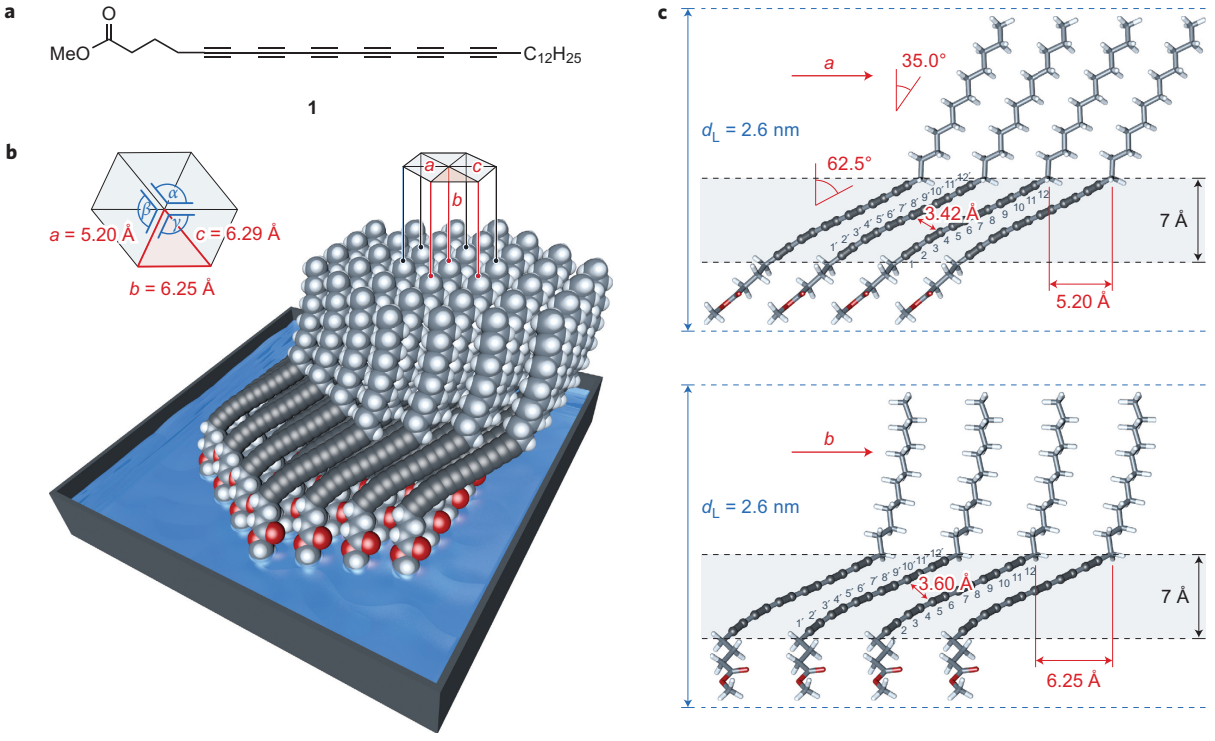

Figure 1 | Well-ordered monolayer of the hexayne amphiphile 1 at the air/water interface. a, Molecular structure of the carbon-rich hexayne amphiphile **1** that was found to self-assemble into monolayers at the air/water interface. **b**, A structural model based on IRRA spectroscopy, the XR and GIXD results, and after geometry optimization by DFT computations. The molecules assumed a distorted hexagonal 2D lattice ($a = 5.20$ Å, $b = 6.25$ Å, $c = 6.29$ Å, $\alpha = 131.0°$, $\beta = 114.9°$, $\gamma = 114.1°$) with spacings determined by the size of the polar head group hydrated with two water molecules (not shown). **c**, The hexayne and dodecyl segments are closely packed with tilt angles of 62.5° and 35.0° relative to the layer normal, which results in an overall layer thickness of $d_L = 2.6$ nm. The packing of **1** revealed numerous carbon–carbon short contacts between the acetylene carbons of neighbouring molecules, of 3.42–3.53 Å along the *a* axis (between C1–C9 and C4′–C12′) and 3.60–3.78 Å along the *b* axis (between C3–C8 and C7′–C12′); only the shortest contacts are shown. The tight packing of the hexaynes within this <7 Å thick 'carbon precursor' sublayer was suitable for quantitative carbonization on ultraviolet irradiation at room temperature.

Negishi-type protocol for the efficient direct coupling of two *sp*-hybridized carbon atoms (Supplementary Fig. 1)[34,35]. Langmuir films were then prepared by spreading dilute solutions of **1** on the surface of Millipore water in a Langmuir trough. Pressure-area isotherms of the films revealed an increase of the surface pressure on compression below a mean molecular area of 24 Å^2, followed by a strongly tilted plateau at surface pressures between 9 and 15 mN m^{-1} and a second steep increase up to the collapse of the film at 37 mN m^{-1} (Supplementary Fig. 2). The compressibility moduli of $C_s^{-1} > 100$ mN m^{-1} and the positions of the asymmetric and symmetric CH_2-stretching vibration bands in infrared reflection–absorption (IRRA) spectra of the film at 2,919 and 2,849 cm^{-1}, respectively, indicated that the molecules were densely packed with the alkyl groups in an ordered *all-trans* state at surface pressures both above and below the plateau (Supplementary Figs 2 and 3)[36,37]. Because the films were less stable above the plateau, all further investigations on the structure and carbonization of the Langmuir films of the hexayne amphiphile **1** were conducted at surface pressures of 8 mN m^{-1}.

The analysis of experimental and simulated IRRA spectra of the films, specular X-ray reflectivity (XR) experiments, as well as grazing incidence X-ray diffraction (GIXD) measurements, allowed us to develop a detailed model of the molecular packing of **1** within the films, which corroborated that it is suitable for subsequent carbonization. From a global fit of experimental IRRA spectra of the film recorded at different angles of incidence with both p- and s-polarized light and spectra simulated on the basis of the optical model of Kuzmin and co-workers[38,39], we were able to determine the layer thickness and the tilt angles of the hexayne and the dodecyl segments of **1** with respect to the surface-layer normal[40]. Thus, from the fit of the intensity of the OH-stretching vibration ν(OH) of the subphase we calculated an effective layer thickness above the subphase of $d_L = 2.2$ nm (Fig. 2a,b and Supplementary Fig. 4). Assuming an extended molecular length of **1** of about 3.7 nm, this finding is consistent with the presence of a monolayer and suggests an average molecular tilt angle of 54° relative to the surface-layer normal. Analogously, fitting the simulated to the experimental band intensities of the symmetric CH_2-stretching and the hexayne vibrations at 2,849 cm^{-1} and 2,200 cm^{-1} resulted in tilt angles of 35° and 62.5° for the dodecyl residue and the hexayne segment, respectively (Fig. 2c,d and Supplementary Figs 5 and 6). These values are in excellent agreement with a close packing of the hexayne and dodecyl segments, considering their different respective cross-sectional areas, and result in virtually the same effective layer thickness as that determined independently from the OH-stretching vibration.

Our interpretation of the IRRA spectroscopy data was supported by an analysis of the electron-density distribution in the monolayer by means of specular XR experiments (Fig. 3a,b and Supplementary Fig. 7), from which we derived an overall layer thickness of $d_L = 2.65$ nm, which included a sublayer thickness of 1.2 nm for the dodecyl segment. The slightly larger film thickness and resulting smaller average molecular tilt of 44° obtained by XR compared to the IRRA spectroscopy data can be explained by the contribution of the hydrated head group of amphiphile **1**. Moreover, the tilt angle of 38° obtained for the dodecyl segment with a length of 1.52 nm in an *all-trans* conformation is in excellent agreement with the IRRA spectroscopy data. These findings were confirmed

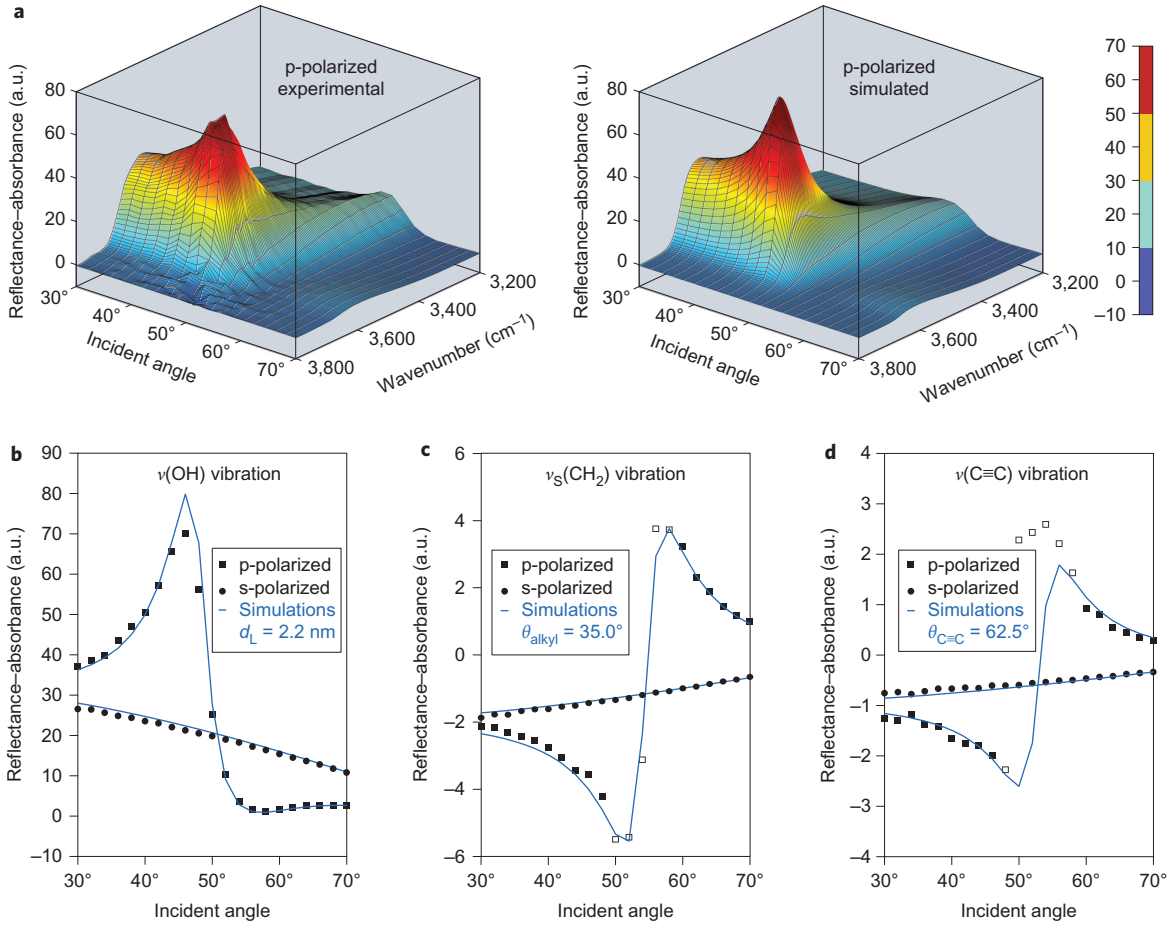

Figure 2 | Fitting of the experimental IRRA spectra for a layer of 1 at the air/water interface. a, Surface plots of the intensity (colour coded) of the OH-stretching vibration ν(OH) of the aqueous subphase as a function of the incident angle for the experimental and simulated spectra in p-polarized light. **b**–**d**, The corresponding plots of the experimental and simulated reflectance–absorbance intensities at the position of the OH-stretching vibration ν(OH) of the subphase, the symmetric CH_2-stretching vibration $\nu_s(CH_2)$ and the hexayne vibration ν(C≡C) (open symbols are not included in the fit). Layer thickness and tilt angles were determined from the best fit of the simulated spectra to the experimental spectra (open symbols were omitted from the fit). (See Supplementary Figs 4–6 for more details.)

further by the synchrotron GIXD data obtained from a monolayer of **1** at the air/water interface (Fig. 3d–i). Owing to the possible partial carbonization of the films in the synchrotron X-ray beam, the data were fitted as a composite of two coexisting structures that represented the uncarbonized and the partially carbonized film. Each structure exhibited three Bragg peaks (Supplementary Figs 8 and 9), which indicated an oblique unit cell. The lattice parameters of the uncarbonized film determined from the diffraction data corresponded to a distorted hexagonal packing with $a = 5.20$ Å, $b = 6.25$ Å, $c = 6.29$ Å, $\alpha = 131.0^\circ$, $\beta = 114.9^\circ$ and $\gamma = 114.1^\circ$ (Fig. 1b). Moreover, an average tilt angle of the hexayne and the dodecyl segments of 52° with respect to the surface-layer normal was obtained (Supplementary Tables 1 and 2), in excellent agreement with the IRRA spectroscopy and XR experiments.

Thus, both the spectroscopy and diffraction experiments confirmed unambiguously the presence of a monolayer of **1** that comprised a densely packed array of the hexayne amphiphiles with the alkyl chains in an ordered *all-trans* state. To further elucidate the molecular packing, in particular with regard to the experimentally inaccessible dihedral angles between the head group, and the hexayne and dodecyl segments, we performed geometry optimizations by DFT computations at the PBE-D2 level with periodic boundary conditions and fixed unit-cell dimensions based on the experimental GIXD results. The obtained energy-optimized structure revealed hexayne segments that were slightly bent (Fig. 1b,c), but much less so than often observed in single crystals of oligoynes with sterically demanding head groups[41,42]. The computations showed that this bending, as well as the adjustment of the individual tilt and dihedral angles, allowed the molecules to better accommodate the different segments' steric demand and thereby resulted in an optimized arrangement of the amphiphiles. The optimized monolayer exhibited a thickness of 2.4 nm (without the experimentally observed hydrating water molecules) and tilt angles of 61.9° and 27.0° for the hexayne and dodecyl segments, respectively, in excellent agreement with the experimental values. Most importantly, however, the optimized structure revealed a very tight packing of the hexayne segments with a whole series of close carbon–carbon short contacts of 3.42–3.53 Å between acetylene carbons C1–C9 and C4′–C12′ (along the *a* axis) and 3.60–3.78 Å between acetylene carbons C3–C8 and C7′–C12′ (along the *b* axis) of neighbouring molecules (Fig. 1c and Supplementary Fig. 10). In other words, the tight and 2D arrangement of the reactive hexayne segments observed in the monolayers of **1** may be considered as a less than 7 Å thick 'carbon precursor' sublayer, with the reactive carbon distances well below the threshold of 4 Å known from topochemical diacetylene polymerization[43,44], and hence well-suited for an extensive irradiation-induced 2D carbonization.

Accordingly, the complete carbonization of the hexayne layer in the films of **1** at the air/water interface was accomplished successfully by crosslinking through ultraviolet irradiation at room

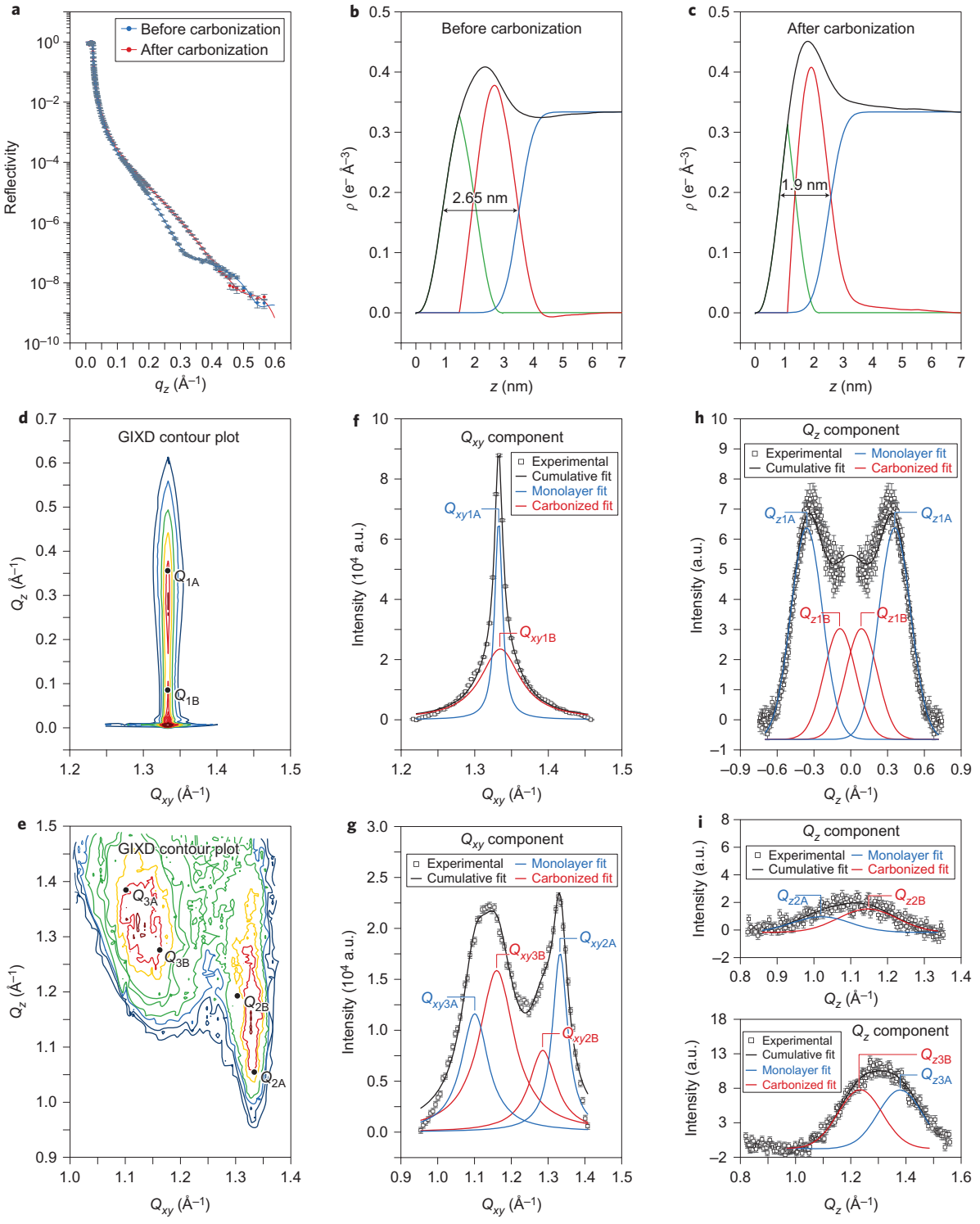

Figure 3 | XR measurements as well as GIXD data for a layer of amphiphile 1. a, Specular XR data of amphiphile **1** at the air/water interface before (blue) and after (red) ultraviolet irradiation at a surface pressure of 8 mN m^{-1} with the corresponding fits (solid lines). **b**,**c**, The corresponding electron-density profiles along the surface normal *z* of a layer of the films before (**b**) and after (**c**) carbonization, fitted by contributions of the dodecyl segment (green) and the residual molecule (red), assuming a root-mean-square roughness of 4 Å of the water subphase (blue). **d**,**e**, Contour plots of the corrected GIXD intensities as a function of the in-plane (Q_{xy}) and out-of-plane (Q_z) scattering vector components, as well as (**f**–**i**) Q_{xy} and Q_z plots of the scattering intensities integrated over a certain Q_z window (**f**,**g**) and a certain Q_{xy} window (**h**,**i**), respectively. The Q_{xy} plots show the Bragg peaks and the Q_z plots the Bragg rods of three diffraction peaks of two coexisting structures (presumably from the uncarbonized and partially carbonized monolayers, labelled as A and B, respectively). (See Supplementary Figs 7–9 and Supplementary Tables 1 and 2 for details.)

temperature. The progress of this irradiation-induced carbonization was monitored by the intensity of the hexayne band at 2,200 cm^{-1} in the IRRA spectra and revealed that the conversion of the hexayne moiety was virtually complete after about 40 minutes of ultraviolet irradiation, although the presence of a small fraction of residual isolated triple bonds cannot be excluded. The derived pseudo-kinetic

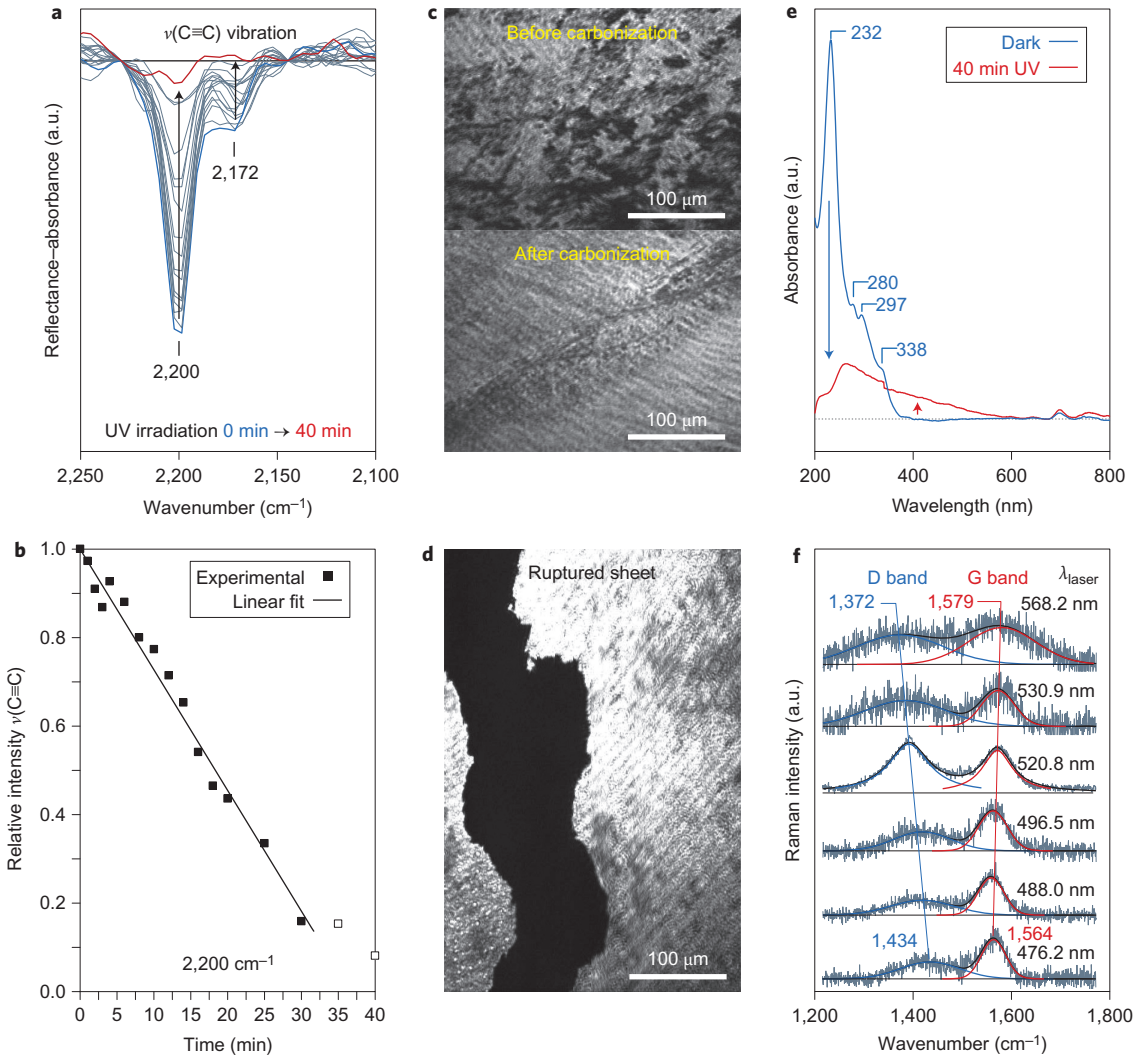

Figure 4 | Carbonization process of a film of 1 monitored by IRRA spectroscopy and characterization of the carbonized films by BAM as well as UV/vis and Raman spectroscopy. a, IRRA spectra of the film before (blue line) and after 1–40 minutes (grey and red lines) of ultraviolet irradiation showed that the bands of the hexayne segment (2,200 and 2,172 cm^{-1}) completely disappeared on ultraviolet irradiation. **b**, A pseudo-kinetic plot of the hexayne band intensity versus irradiation time showed a linear relationship up to conversions above 80% (open squares represent experimental values not considered in the linear fit). **c**,**d**, Brewster angle micrographs of the carbon nanosheets after ultraviolet irradiation showed a uniform film that could only be ruptured by violent manipulation. **e**, UV-vis spectra of irradiated films transferred to a sapphire substrate showed a broad and featureless absorption at wavelengths up to 600 nm. **f**, Raman spectroscopy on multilayered material transferred to SiO_2 substrates gave rise to the signature Raman bands of carbon materials. (See Supplementary Figs 11–14 for details.)

plot of band intensity versus irradiation time showed a linear relationship up to acetylene conversions of more than 80%. To interpret this observation as pseudo zero-order kinetics would imply that the carbonization process does not (solely) rely on the excitation of hexayne monomers (Fig. 4a,b and Supplementary Fig. 11). Brewster angle microscopy (BAM) experiments showed a change in the texture of the films on ultraviolet irradiation. The new texture was maintained, and no defects were observed in the carbonized films, even after expansion of the barriers and reduction of the surface pressure. A rupture of the carbonized films was only achieved by violent manipulation with a needle, which left large islands floating at the air/water interface, and provided an indication of the hugely increased mechanical stability of the monolayers after carbonization (Fig. 4c,d and Supplementary Fig. 12).

Interestingly, the surface pressure at the air/water interface was found to increase during the course of the carbonization for monolayers irradiated at a constant surface area. Consistently, a significant expansion of the surface area was observed when the experiment was performed at constant surface pressure (Supplementary Fig. 13). This lateral expansion of the monolayer on carbonization indicates that a further planarization of the acetylenic carbons in the precursor layer takes place during this transformation. If the density of the carbon sublayer changes at all, it is expected to increase as a result of the covalent crosslinking. Consequently, its thickness can be estimated to be reduced from 7 Å to well below 6 Å, which is the upper bound estimated from the 15% increase in surface area. Indeed, XR experiments confirmed that the carbonization of the Langmuir films of **1** was accompanied by a vertical contraction of the overall layer thickness from 2.65 to 1.9 nm (Fig. 3c). This significantly reduced layer thickness is the combined result of the vertical contraction of the carbon sublayer described above and a concomitant rearrangement of the dodecyl segments as a consequence of the lateral expansion of the film. Thus, the bands for the asymmetric and symmetric CH_2-stretching vibrations shifted to 2,924 and 2,855 cm^{-1},

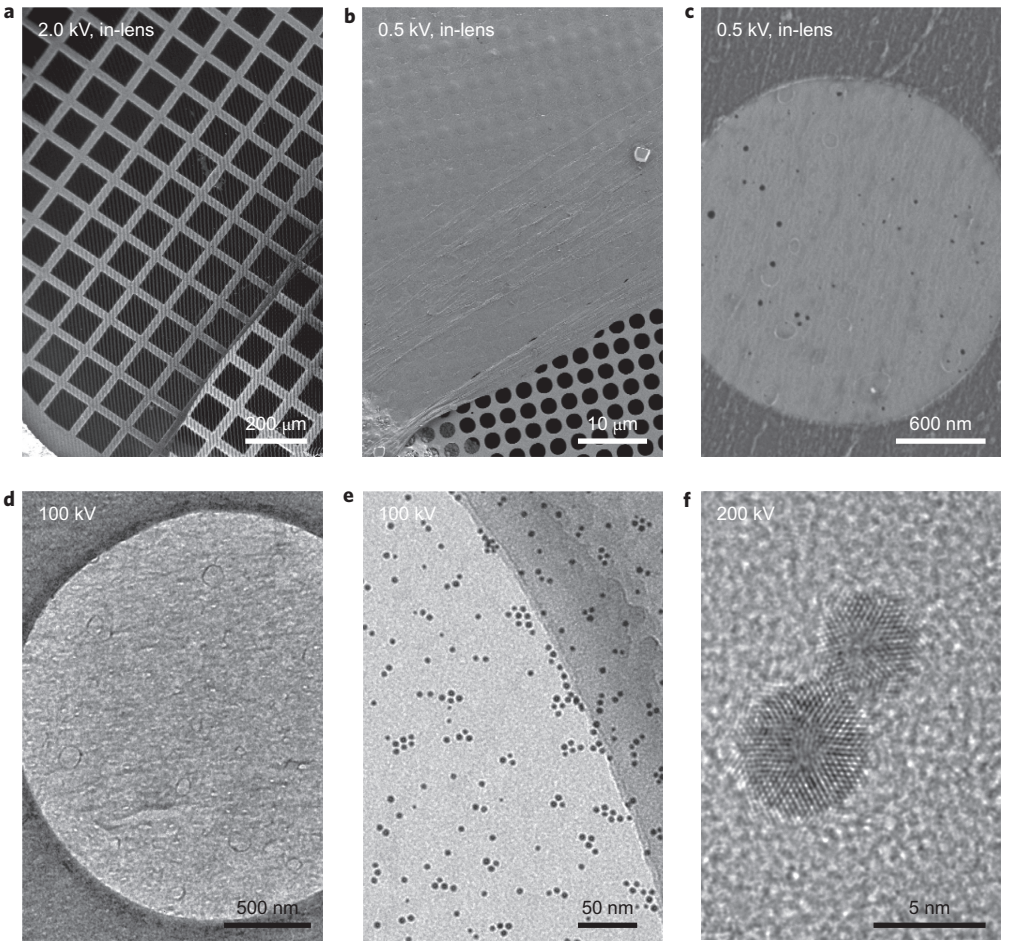

Figure 5 | SEM and TEM images of carbon nanosheets obtained by carbonization of 1 at the air/water interface after transfer to a holey carbon TEM grid. a,**b**, A partially covered grid revealed a slight contrast difference at an accelerating voltage of 2.0 kV (**a**), and the carbon nanosheets became opaque at 0.5 kV (**b**). **c**, High-resolution SEM images showed small circular holes in the carbon nanosheets and some blisters on its surface. **d**, TEM images revealed the corrugated structure of the carbon nanosheets, which can be discriminated against the background of the carbon frames of the TEM grid. **e**, The carbon nanosheets served as a substrate for hydrophilic gold nanoparticles deposited by drop-casting from an aqueous solution. Comparison with image regions on the 10–12 nm thick carbon of the holey carbon TEM grid highlights the very low background contrast provided by the 2 nm thick carbon nanosheets. **f**, The carbon nanosheets were sufficiently stable to serve as support films under the strong electron beam (200 kV) conditions in HR-TEM, and the obtained images showed the fringes of the lattice planes of the gold nanoparticles. (See Supplementary Figs 15–19 for details.)

respectively, positions characteristic for alkyl chains in a liquid-expanded state (Supplementary Fig. 11)[37]. Consistent with this loss of in-plane ordering in the hexayne and dodecyl segments throughout the ultraviolet-induced carbonization, GIXD experiments performed on carbonized films did not show any diffraction peaks.

Ultraviolet/visible (UV/vis) and Raman spectroscopy on irradiated Langmuir films of **1** transferred to solid substrates provided conclusive evidence for the extensive carbonization and formation of sp^2-rich carbon nanosheets. UV/vis spectra on films transferred to sapphire substrates showed a broad, featureless absorption at wavelengths of up to 600 nm after the ultraviolet-induced carbonization, but lacked the absorption bands of the hexayne chromophore in the range $\lambda = 232–338$ nm (Fig. 4e). The main absorbance peak of the carbon nanosheets at ~260 nm is consistent with the reported characteristic position for spectra of reduced graphene oxide and has been attributed to the $\pi–\pi^*$ transition of the carbon–carbon double bonds[45,46]. Moreover, the optical bandgap of approximately 2.2 eV at the observed absorption edge of about 550 nm suggested, according to studies of graphene oxide materials, the presence of at least nanometre-sized graphene-like domains[45,46]. At the same time, background-corrected multiwavelength Raman spectra on material transferred to SiO_2 substrates revealed the G and D bands (1,562 and 1,478 cm^{-1} at a laser excitation wavelength $\lambda_{ex} = 496.5$ nm) characteristic for sp^2-rich carbon materials (Fig. 4f and Supplementary Fig. 14). The signal-to-noise ratio of the spectra was affected strongly by the photoluminescence background typical for such carbon materials[47,48] and appeared to be subject to a resonance enhancement close to the absorption edge of the carbon nanosheets, which lends further credence to the interpretation of the absorption spectra. A detailed analysis of the positions and intensities of the G and D bands as a function of the laser excitation wavelength allowed us to conclude that the carbon microstructure consisted mainly of extended sp^2-hybridized carbon clusters (>80%) with a minor amount of 'edge states' connected to sp^3-hybridized carbon centres (10–15%). The presence of small fractions of *sp*-hybridized carbons from isolated triple bonds cannot be fully excluded. We have, hence, produced carbon nanosheets in ambient conditions that are extensively conjugated and closely resemble 'amorphous carbon' materials obtained under conditions well above the onset of graphitization at typical annealing temperatures above 800–1,000 °C[49–52], and it is tempting to assign the observed fraction of 10–15% 'edge states' to the two carbons (of the 12 former acetylene carbons) connected covalently to the dodecyl termini and head groups, respectively. On the basis

of its thickness, the absorption spectra and Raman results, we may thus contemplate a tentative structure model for the carbon sublayer akin to reduced graphene oxide, with a crosslinked and defect-rich network of at least nanometre-sized graphene 'flakes' that are oriented, on average, parallel to the air/water interface.

Furthermore, the carbon nanosheets were characterized by both scanning and transmission electron microscopy (SEM and TEM) after transfer to a holey carbon TEM grid as support. The contrast between the free and covered parts of the grid in SEM images taken with the in-lens detector at low working distances was only discernible at acceleration voltages of 2.0 kV and below (Fig. 5a). The films became opaque to the electron beam on further reducing the voltage to 0.5 kV, and the images revealed carbon nanosheets that spanned the $2 \times 2\ \mu m^2$ sized holes of the grid with only a few defects (Fig. 5b). Both SEM and TEM micrographs showed that the film was partially draped and wrinkled at its edge, and very smooth further away from the border (Supplementary Figs 15–17). Small circular holes of a few nanometres in diameter were visible in high-resolution SEM images of the free-standing carbon nanosheets, as well as some blisters on the surface of the films that otherwise appeared uniform and smooth (Fig. 5c). Although carbon materials with a typical knock-on voltage of 80 kV or lower usually suffer from beam damage at these voltages in TEM[53,54], concentrating the full power of the electron beam in one spot only resulted in the slow growth of holes already present in the carbon film and not a rupture of the films.

Moreover, the carbon nanosheets offered a very low background contrast and a functionalized hydrophilic surface, which led us to investigate their use as substrates for TEM imaging of other specimens, as had been reported previously for graphene-oxide substrates[55]. To this end, we drop-cast an aqueous solution of 4.4 nm sized gold nanoparticles coated with hydrophilic ligands onto a holey carbon TEM grid covered with a carbon nanosheet obtained by carbonization of **1** at the air/water interface, and imaged the deposited nanoparticles with TEM (Fig. 5 and Supplementary Figs 18 and 19). The results demonstrated that the carbon nanosheets were a sufficiently stable support for the nanoparticles, even under the 200 kV electron-beam conditions employed in high-resolution TEM (HR-TEM) imaging that showed the gold nanoparticles and the fringes of the gold lattice planes with high contrast (Fig. 5f). With a hydrophilic surface functionalization and the defined thickness of less than 2 nm, the carbon nanosheets provided a solid self-supporting substrate with properties compatible with those of the hydrophilic specimen, without a treatment such as glow discharge, and offered an extraordinarily low background contrast to give a light texture, illustrated by comparison with image regions with the 10–12 nm thick carbon frames of the holey carbon TEM grids (Fig. 5e).

Conclusions

In conclusion, we have developed a novel approach for the preparation of thin, 2D carbon nanostructures with extended lateral dimensions based on the self-assembly and subsequent carbonization of the hexayne amphiphile **1** at the air/water interface. A detailed molecular model of the monolayer's internal structure provided strong evidence that the hexayne moieties were densely packed at the $\pi-\pi$ stacking distance, suitable for carbonization. Subsequent ultraviolet irradiation of the films resulted in complete carbonization of the molecular precursors at room temperature to produce sp^2-rich carbon nanosheets with a carbon microstructure that resembled amorphous carbon materials typically obtained after annealing at temperatures of 800–1,000 °C[49–52]. In this way, we produced mechanically stable and rigid functionalized carbon films that bear similarities to reduced graphene oxide, with a molecularly defined overall thickness of 1.9 nm and lateral dimensions on the order of centimetres that are, presumably, only limited by the dimensions of the Langmuir trough. These thin carbon nanosheets with their hydrophilic surface functionalization proved to be useful as low background-contrast substrates for the HR-TEM imaging of specimens deposited from aqueous media. The possibility to prepare large functional carbon nanosheets under benign conditions opens new avenues for applications such as chemoselective electron-microscopy substrates, protective coatings, transparent and conformal electrodes, and membrane materials.

Methods

A comprehensive account of all experimental details, including Supplementary Figs 1–20, Supplementary Tables 1 and 2, experimental procedures and analytical data for all compounds, as well as computational details, is provided in the Supplementary Information.

Langmuir technique, monolayer preparation and ultraviolet-induced carbonization. Pressure-area isotherms were recorded on a Langmuir trough equipped with movable barriers and a surface-pressure microbalance (R&K) with a filter paper Wilhelmy plate. An external thermostat (E1 Medingen) was used to maintain the temperature of the subphase at 20 °C. The Langmuir trough was placed in a sealed box to avoid contamination of the interface. Langmuir films were prepared by spreading solutions of **1** in dichloromethane/chloroform (1:25, $c = 1\ mmol\ l^{-1}$) on Millipore water with a Hamilton syringe (Model 1810 RN SYR). For carbonization experiments, ultraviolet irradiation was carried out using a 250 W Ga-doped low-pressure Hg lamp (UV-Light Technology) placed 50 cm away from the air/water interface.

IRRA spectroscopy. Spectra were recorded on a Vertex 70 FT-IR spectrometer from Bruker equipped with a liquid-nitrogen cooled mercury cadmium telluride detector attached to an external air–water reflection unit (XA-511 Bruker). The infrared beam was focused onto the water surface of the trough and the measurements were carried out with p- and s-polarized light at different angles of incidence above and below the Brewster angle. A trough with two compartments in a hermetically sealed box was used. One compartment contained the system under investigation (sample), and the other was filled with the pure subphase (reference), and the trough was shuttled for illumination. The single-beam reflectance spectrum from the reference trough was taken as background for the single-beam reflectance spectrum from the sample trough to yield the reflection–absorption spectrum as $\log(R/R_0)$ and eliminate the water-vapour signal. The incident infrared beam was polarized with a KRS-5 wire-grid polarizer. For s-polarized light, spectra were co-added over 200 scans, and spectra with p-polarized light were co-added over 400 scans. The resolution and scanner speed in all experiments were 8 cm^{-1} and 20 kHz, respectively. Spectra were shifted to a common baseline for comparison.

Simulation and fitting of IRRA spectra. IRRA spectra were simulated using a MATLAB program on the basis of the optical model of Kuzmin and co-workers[38,39], which was adapted for the simulation of spectra with multiple bands[40]. The intensity and shape of a reflection absorption band depend on the absorption coefficient k, the full-width at half-height (FWHH), the orientation of the transition dipole moment within the molecule α, the molecular tilt angle θ, the polarization and the angle of incidence (AoI) of the incoming light, as well as the layer thickness d and its refractive index n. Simulated spectra were fitted to the experimental data in a global fit, in which all spectra recorded at different AoIs and different polarizations were fitted in one nonlinear least-square minimization using the Levenberg–Marquardt algorithm. The layer thickness d and the refractive index n were determined from a fit of the OH-stretching vibrational band (ν(OH)). The determined values were then set constant, and the symmetrical CH_2-stretching vibrational band ($\nu_s(CH_2)$) as well as the acetylene stretching vibrational band (ν(C≡C)) were fitted using an angle α of 90° and 0°, respectively. Fitting parameters for these bands were k, FWHH and the tilt angle of the respective molecular moieties θ. The spectra taken with p-polarization and angles of incidence between 50° and 58° were omitted from the fit because of the low reflectivity of the monolayer near the Brewster angle. The spectra were shifted to a common baseline at 3,800, 2,800 and 2,218 cm^{-1} for the fit of the ν(OH), $\nu_s(CH_2)$ and ν(C≡C) bands, respectively.

GIXD. These measurements were carried out at the undulator beamline BW1 using the liquid-surface diffractometer at HASYLAB, DESY (for full experimental details see the Supporting Information). The GIXD set-up was equipped with a temperature-controlled Langmuir trough (R&K), which was enclosed in a sealed, helium-filled container. The trough was thermostatted at 10 °C for diffraction experiments with monolayers of **1**. The synchrotron X-ray beam was monochromatted to a wavelength of 1.304 Å (beryllium (002) crystal) and adjusted to strike the helium–water interface at a grazing incidence angle of $\alpha_i = 0.85\ \alpha_c$ ($\alpha_c = 0.13°$ is the critical angle for total reflection), which illuminated approximately $2 \times 50\ mm^2$ of the monolayer surface. A MYTHEN detector system (PSI) was used to measure the diffracted signal and was rotated to scan the in-plane Q_{xy} component values of the scattering vector. A Soller collimator in front of the MYTHEN detector restricted the in-plane divergence of the diffracted beam to 0.09°. The vertical strips of the MYTHEN detector measured the out-of-plane Q_z component of the scattering

vector between 0.0 and 0.75 $Å^{-1}$. The diffraction data consisted of Bragg peaks at diagnostic Q_{xy} values obtained by summing the diffracted intensity over a defined vertical angle or Q_z window. The in-plane lattice-repeat distances d of the ordered structures in the monolayer were calculated from the Bragg peak positions, $d = 2\pi/Q_{xy}$. To estimate the extent of the crystalline order in the monolayer, the in-plane coherence length L_{xy} was approximated from the full-width at half-maximum (FWHM) of the Bragg peaks using $L_{xy} \approx 0.9(2\pi)/\mathrm{FWHM}(Q_{xy})$ using the measured $\mathrm{FWHM}(Q_{xy})$ corrected for the instrumental resolution. Integrating the diffracted intensity normal to the interface over the Q_{xy} window of the diffraction peak yielded the corresponding Bragg rod. The thickness of the scattering unit was estimated from the FWHM of the Bragg rod using $0.9(2\pi)/\mathrm{FWHM}(Q_z)$.

Specular XR. These experiments were carried out at the liquid-surface diffractometer on the undulator beamline BW1 (HASYLAB, DESY). The reflected intensity was measured by a NaI scintillation detector as a function of the vertical incidence angle α_i, with the geometry $\alpha_i = \alpha_f = \alpha$, where α_f is the vertical exit angle of the reflected X-rays. The vertical scattering vector component $Q_z = (4\pi/\lambda)\sin\alpha_r$ was measured in a range between 0.01 and 0.65 $Å^{-1}$. The background scattering from, for example, the subphase, was measured at $2\theta_{hor} = 0.7^\circ$ (off-specular) and subtracted from the signal measured at $2\theta_{hor} = 0^\circ$ (specular), with $2\theta_{hor}$ as the angle between the horizontal projection of the incident and reflected beam. The reflectivity data were inverted by applying a model-independent approach, including linear combinations of *b*-splines (see the Supplementary Information for more details). The obtained electron-density profile was interpreted by assuming two Gaussian-shaped electron-density distributions.

References

1. Novoselov, K. S. *et al.* Electric field effect in atomically thin carbon films. *Science* **306,** 666–669 (2004).
2. Geim, A. K. & Novoselov, K. S. The rise of graphene. *Nature Mater.* **6,** 183–191 (2007).
3. Angelova, P. *et al.* A universal scheme to convert aromatic molecular monolayers into functional carbon nanomembranes. *ACS Nano* **7,** 6489–6497 (2013).
4. Matei, D. G. *et al.* Functional single-layer graphene sheets from aromatic monolayers. *Adv. Mater.* **25,** 4146–4151 (2013).
5. Guldi, D. M. & Sgobba, V. Carbon nanostructures for solar energy conversion schemes. *Chem. Commun.* **47,** 606–610 (2011).
6. Burghard, M., Klauk, H. & Kern, K. Carbon-based field-effect transistors for nanoelectronics. *Adv. Mater.* **21,** 2586–2600 (2009).
7. Rogers, J. A., Lagally, M. G. & Nuzzo, R. G. Synthesis, assembly and applications of semiconductor nanomembranes. *Nature* **477,** 45–53 (2011).
8. Sekitani, T. & Someya, T. Stretchable, large-area organic electronics. *Adv. Mater.* **22,** 2228–2246 (2010).
9. Unarunotai, S. *et al.* Conjugated carbon monolayer membranes: methods for synthesis and integration. *Adv. Mater.* **22,** 1072–1077 (2010).
10. van der Zande, A. M. *et al.* Large-scale arrays of single-layer graphene resonators. *Nano Lett.* **10,** 4869–4873 (2010).
11. Ang, P. K. *et al.* A bioelectronic platform using a graphene–lipid bilayer interface. *ACS Nano* **4,** 7387–7394 (2010).
12. Georgakilas, V. *et al.* Functionalization of graphene: covalent and non-covalent approaches, derivatives and applications. *Chem. Rev.* **112,** 6156–6214 (2012).
13. Hoheisel, T. N., Schrettl, S., Szilluweit, R. & Frauenrath, H. Nanostructured carbonaceous materials from molecular precursors. *Angew. Chem. Int. Ed.* **49,** 6496–6515 (2010).
14. Mas-Balleste, R., Gomez-Navarro, C., Gomez-Herrero, J. & Zamora, F. 2D materials: to graphene and beyond. *Nanoscale* **3,** 20–30 (2011).
15. Yuan, C. Z. *et al.* Hierarchically structured carbon-based composites: design, synthesis and their application in electrochemical capacitors. *Nanoscale* **3,** 529–545 (2011).
16. Li, X. *et al.* Large-area synthesis of high-quality and uniform graphene films on copper foils. *Science* **324,** 1312–1314 (2009).
17. Sun, Z. *et al.* Growth of graphene from solid carbon sources. *Nature* **468,** 549–552 (2010).
18. Liu, H. T. *et al.* Photochemical reactivity of graphene. *J. Am. Chem. Soc.* **131,** 17099–17101 (2009).
19. Sinitskii, A. *et al.* Kinetics of diazonium functionalization of chemically converted graphene nanoribbons. *ACS Nano* **4,** 1949–1954 (2010).
20. Georgakilas, V. *et al.* Organic functionalisation of graphenes. *Chem. Commun.* **46,** 1766–1768 (2010).
21. Wang, X. R., Tabakman, S. M. & Dai, H. J. Atomic layer deposition of metal oxides on pristine and functionalized graphene. *J. Am. Chem. Soc.* **130,** 8152–8153 (2008).
22. An, X. H. *et al.* Stable aqueous dispersions of noncovalently functionalized graphene from graphite and their multifunctional high-performance applications. *Nano Lett.* **10,** 4295–4301 (2010).
23. Zasadzinski, J. A., Viswanathan, R., Madsen, L., Garnaes, J. & Schwartz, D. K. Langmuir–Blodgett films. *Science* **263,** 1726–1733 (1994).
24. Ulman, A. Formation and structure of self-assembled monolayers. *Chem. Rev.* **96,** 1533–1554 (1996).
25. Sakamoto, J., van Heijst, J., Lukin, O. & Schluter, A. D. Two-dimensional polymers: just a dream of synthetic chemists? *Angew. Chem. Int. Ed.* **48,** 1030–1069 (2009).
26. Gros, L., Ringsdorf, H. & Schupp, H. Polymeric antitumor agents on a molecular and on a cellular level? *Angew. Chem. Int. Ed. Engl.* **20,** 305–325 (1981).
27. Chechik, V., Crooks, R. M. & Stirling, C. J. M. Reactions and reactivity in self-assembled monolayers. *Adv. Mater.* **12,** 1161–1171 (2000).
28. Scott, J. C., Samuel, J. D. J., Hou, J. H., Rettner, C. T. & Miller, R. D. Monolayer transistor using a highly ordered conjugated polymer as the channel. *Nano Lett.* **6,** 2916–2919 (2006).
29. Szilluweit, R. *et al.* Low-temperature preparation of tailored carbon nanostructures in water. *Nano Lett.* **12,** 2573–2578 (2012).
30. Néabo, J. R., Vigier-Carrière, C., Rondeau-Gagné, S. & Morin, J-F. Room-temperature synthesis of soluble, fluorescent carbon nanoparticles from organogel precursors. *Chem. Commun.* **48,** 10144–10146 (2012).
31. Ding, L. & Olesik, S. V. Synthesis of polymer nanospheres and carbon nanospheres using the monomer 1,8-dihydroxymethyl-1,3,5,7-octatetrayne. *Nano Lett.* **4,** 2271–2276 (2004).
32. Luo, L. *et al.* Room-temperature carbonization of poly(diiodobiacetylene) by reaction with Lewis bases. *J. Am. Chem. Soc.* **133,** 19274–19277 (2011).
33. Levesque, I. *et al.* Layered graphitic materials from a molecular precursor. *Chem. Sci.* **5,** 831–836 (2014).
34. Hoheisel, T. N. & Frauenrath, H. A convenient Negishi protocol for the synthesis of glycosylated oligo(ethynylene)s. *Org. Lett.* **10,** 4525–4528 (2008).
35. Hoheisel, T. N. *et al.* A multistep single-crystal-to-single-crystal bromodiacetylene dimerization. *Nature Chem.* **5,** 327–334 (2013).
36. Davies, J. T. & Rideal, E. K. *Interfacial Phenomena* 2nd edn (Academic Press, 1963).
37. Mendelsohn, R., Mao, G. & Flach, C. R. Infrared reflection–absorption spectroscopy: principles and applications to lipid–protein interaction in Langmuir films. *Biochim. Biophys. Acta Biomembranes* **1798,** 788–800 (2010).
38. Kuzmin, V. L. & Mikhailov, A. V. Molecular theory of light reflection and applicability limits of the macroscopic approach. *Opt. Spectrosc. (USSR)* **51,** 383–385 (1981).
39. Kuzmin, V. L., Romanov, V. P. & Michailov, A. V. Reflection of light at the boundary of liquid systems and structure of the surface layer: a review. *Opt. Spectrosc.* **73,** 1–26 (1992).
40. Schwieger, C., Chen, B., Tschierske, C., Kressler, J. & Blume, A. Organization of T-shaped facial amphiphiles at the air/water interface studied by infrared reflection absorption spectroscopy. *J. Phys. Chem. B* **116,** 12245–12256 (2012).
41. Szafert, S. & Gladysz, J. A. Update 1 of: Carbon in one dimension: structural analysis of the higher conjugated polyynes. *Chem. Rev.* **106,** PR1–PR33 (2006).
42. Chalifoux, W. A. & Tykwinski, R. R. Synthesis of polyynes to model the *sp*-carbon allotrope carbyne. *Nature Chem.* **2,** 967–971 (2010).
43. Baughman, R. H. Solid-state synthesis of large polymer single crystals. *J. Polym. Sci. Polym. Phys. Ed.* **12,** 1511–1535 (1974).
44. Enkelmann, V. Structural aspects of the topochemical polymerization of diacetylenes. *Adv. Polym. Sci.* **63,** 91–136 (1984).
45. Eda, G. *et al.* Blue photoluminescence from chemically derived graphene oxide. *Adv. Mater.* **22,** 505–509 (2010).
46. Kumar, P. V. *et al.* Scalable enhancement of graphene oxide properties by thermally driven phase transformation. *Nature Chem.* **6,** 151–158 (2014).
47. Cao, L., Meziani, M. J., Sahu, S. & Sun, Y-P. Photoluminescence properties of graphene versus other carbon nanomaterials. *Acc. Chem. Res.* **46,** 171–180 (2013).
48. Veca, L. M. *et al.* Polymer functionalization and solubilization of carbon nanosheets. *Chem. Commun.* 2565–2567 (2009).
49. Ferrari, A. C. & Robertson, J. Interpretation of Raman spectra of disordered and amorphous carbon. *Phys. Rev. B* **61,** 14095–14107 (2000).
50. Ferrari, A. C. & Robertson, J. Resonant Raman spectroscopy of disordered, amorphous, and diamondlike carbon. *Phys. Rev. B* **64,** 075414 (2001).
51. Casiraghi, C., Ferrari, A. C. & Robertson, J. Raman spectroscopy of hydrogenated amorphous carbons. *Phys. Rev. B* **72,** 085401 (2005).
52. Falcao, E. H. L. & Wudl, F. Carbon allotropes: beyond graphite and diamond. *J. Chem. Technol. Biotechnol.* **82,** 524–531 (2007).
53. Börrnert, F. *et al.* Amorphous carbon under 80 kV electron irradiation: a means to make or break graphene. *Adv. Mater.* **24,** 5630–5635 (2012).
54. Warner, J. H. *et al.* Investigating the diameter-dependent stability of single-walled carbon nanotubes. *ACS Nano* **3,** 1557–1563 (2009).
55. Patterson, J. P. *et al.* A simple approach to characterizing block copolymer assemblies: graphene oxide supports for high contrast multi-technique imaging. *Soft Matter* **8,** 3322–3328 (2012).

Acknowledgements

The authors thank I. Berndt for help with the isotherm measurements and E. Bremond for assistance with the IRRA surface plots. Also, F. Stellacci, J. C. Brauer and T. N. Hoheisel are gratefully acknowledged for helpful discussions and comments on the manuscript. Funding from the European Research Council (ERC Grant 239831, 'OrgElNanoCarbMater') is gratefully acknowledged, C.S. thanks the Max Planck Society for a stipend, C.Sch. thanks the DFG for funding within FOR 1145 and C.C. acknowledges the Swiss NSF Grant 200021_121577/1. We thank HASYLAB at DESY, Hamburg, Germany, for beam time and excellent support.

Author contributions

S.S. synthesized all the compounds, performed Langmuir experiments, BAM and IRRA spectroscopy together with C.S., TEM imaging with J.R., SEM imaging with G.P., HR-TEM with E.O. and carried out the carbonization experiments as well as UV/vis spectroscopy. C.S. and G.B contributed the GIXD and specular XR experiments. C.Sch. carried out the simulation, fitting and interpretation of the IRRA spectra. Y.F. performed the Raman spectroscopy supervised by A.FiM. J.R. synthesized the hydrophilic gold nanoparticles. R.P. and C.C. performed the DFT computations. All these authors contributed to writing the manuscript. H.F. had the idea, directed the research and co-wrote the manuscript with S.S.

Additional information

Supplementary information and chemical compound information are available in the online version of the paper. Reprints and permissions information is available online at www.nature.com/reprints. Correspondence and requests for materials should be addressed to H.F.

Competing financial interests

The authors declare no competing financial interests.